

NUMERICAL MODELING OF THE MEDIUM-DENSITY FIBERBOARD HOT PRESSING PROCESS, PART 2: MECHANICAL AND HEAT AND MASS TRANSFER MODELS

Zanin Kavazović[†]

Postdoctoral Fellow
E-mail: zanin.kavazovic.1@ulaval.ca

Jean Deteix

Research Associate
E-mail: deteix@giref.ulaval.ca

André Fortin

Professor
Groupe Interdisciplinaire de Recherche en Éléments Finis
Département de Mathématiques et de Statistique
1045, Avenue de la Médecine, Université Laval
Québec, QC, Canada G1V 0A6
E-mail: afortin@giref.ulaval.ca

Alain Cloutier^{*†}

Professor
Centre de Recherche sur le Bois
Département des Sciences du bois et de la Forêt
2425, Rue de la Terrasse, Université Laval
Québec, QC, Canada G1V 0A6
E-mail: alain.cloutier@sbf.ulaval.ca

(Received September 2011)

Abstract. In this study, coupled mechanical and heat and mass transfer models describing mat compression and heat and moisture transfer occurring during hot pressing of medium-density fiberboard mats are presented. The mat is considered an aging linear elastic material and is described by a mechanical model in three dimensions. Rheological properties of the mat depended on time, space, temperature, moisture content, and resin cure. Hardening and softening phases of the material behavior were accounted for and treated with separate constitutive laws. Press closing was taken into account, and a coupling procedure between mechanical and heat and mass transfer models was elaborated. Development of the vertical density profile was dynamically predicted by the model. Both mechanical and heat and mass transfer models were discretized in space by the finite element method. An implicit second-order backward finite difference scheme was used for time discretization. All calculations were carried out on a moving geometry whose deformation (compression) was a function of a press closing schedule. Model results exhibited good agreement with experimental results. Under various press closing schedules, the model gave information on variables such as density profile, total gas pressure, air and vapor pressure, temperature, moisture content, RH, and degree of resin cure.

Keywords: Mathematical model, hot pressing, coupled mechanical and heat and mass transfer models, coupling, moving domain, finite element method, resin cure dynamics, nonhomogeneous density profile.

* Corresponding author

† SWST member

INTRODUCTION

When a wood composite mat is hot pressed, mechanical deformation and heat and moisture transfer processes are intimately coupled and strongly interact with each other (Nigro and Storti 2001; Zombori et al 2003; Dai and Yu 2004; Thömen and Humphrey 2006; Thömen and Ruf 2008). Dynamical development of the vertical density profile is enhanced by a softening effect of moisture content and heat (Bolton et al 1989; Thömen and Ruf 2008). Conversely, changes in the vertical density profile influence thermal conductivity, gas permeability, and porosity of a composite mat, thus affecting heat and moisture transfer in the mat.

The literature on combined mechanical and heat and mass transfer models of the hot pressing process rarely presents detailed information about the coupling procedure. Among the first researchers proposing an integrated approach were Kavvouras (1977), Humphrey (1982), Bolton and Humphrey (1988), and Humphrey and Bolton (1989). Recently, models have been developed by Dai (2001), Carvalho et al (2003), Zombori et al (2003), Pereira et al (2006), and Thömen et al (2006). Meanwhile, Winistorfer et al (1996, 2000), Wang and Winistorfer (2000a, 2000b), and Wang et al (2001a, 2001b, 2004) published a series of studies presenting gamma ray in situ measurements of the vertical density profile development during hot pressing. Unfortunately, the apparatus needed to conduct those experiments is not commonly available. Therefore, to gain insight into the dynamic development of the vertical density profile, an approach based on numerical simulation appears to be a promising avenue (Thömen et al 2006).

Mechanical behavior of wood-based composites is influenced by moisture content (M) and temperature (T) conditions. Wolcott et al (1990) characterized temperature evolution in the mat during flakeboard hot pressing and its relation with the glass transition of lignin and hemicelluloses. This can explain the development of the vertical density profile during the hot pressing process. This phenomenon can also be related to hygrothermal

aging (time dependence of mechanical properties) inducing dependence of the rheological parameters on evolving M and T . Thus, coupling of the mechanical model with the heat and mass transfer model becomes necessary and helps to describe more accurately the interactions between heat and mass transfer and rheological mechanisms.

The aim of this study was to develop a numerical model of the linear elastic mechanical behavior of an aging medium-density fiberboard (MDF) mat with mechanical properties dependent on time, temperature, moisture content, and resin cure and to describe methodology developed and solution strategy implemented to simulate MDF hot pressing. We propose a global coupled mechanical and heat and mass transfer numerical model based on the finite element method. In Part 1 of this study, equations of conservation of energy, air mass, and water vapor mass were proposed to model heat and mass transfer. This 3D unsteady mathematical model was expressed as a function of three state variables: temperature, air pressure, and water vapor pressure. Assumed boundary conditions, time- and space-dependent material properties of the mat, and numerical solution methods and strategy were also presented. All relevant details regarding the heat and mass transfer model were provided in Part 1. Therefore, we shall only discuss here the mechanical model and its coupling with the heat and mass transfer model. Robustness and flexibility of the global model were tested under various pressing conditions, and the model was used to perform several tests and case studies.

MATERIALS AND METHODS

Results of our coupled numerical model were validated against the same experimental data as those presented in Part 1 of this study. Relevant details regarding materials and panel manufacturing were also presented in Part 1 and shall not be repeated here.

Methods

Interactions between rheological and heat and moisture transfer mechanisms during the hot

pressing of MDF mats contribute to the development of a nonhomogeneous density profile. We propose and describe an approach to couple mechanical and heat and mass transfer models allowing predicting time- and space-dependent development of a vertical density profile. Because material and rheological properties of the mat depend on time, density, resin cure, temperature, and moisture content (aging material) (Appendix 1), coupling of mechanical and heat and mass transfer models is necessary. The proposed models have a general 3D mathematical formulation. A linear elastic model for an aging material was used. Press closing and effect of changing mat thickness on the material and rheological properties of the mat are also taken into account. Numerical procedure combines the finite element method with a quasistatic incremental formulation. Also, the geometry of the working domain evolves during the pressing process. In Part 1 of this study, material (Lagrangian) formulation was adopted and calculations were transferred to a reference domain. In Part 2, however, updated Lagrangian formulation of all equations is used and calculations are carried out on a dynamically moving domain. The mesh grid moves as well and is updated after each time step. Updated Lagrangian formulation enables us to capture the movement of the domain in a natural way. Resolution strategy and coupled mechanical and heat and mass transfer models were integrated into the finite element code MEF++ developed by the Groupe interdisciplinaire de recherche en éléments finis at Laval University, Québec, Canada.

Overall Approach and Assumptions

Expressions and equations describing material properties, sorption model, and resin cure kinetics were obtained from available literature and presented in Appendix 1 of Part 1 of this study. None of the fiber mat material and rheological properties were obtained from panels produced in the laboratory. Expressions of coefficients used in the fourth-order elasticity tensor are based on information presented by Thömen et al (2006) for Burger's model. Those coefficients were first obtained by von Haas (1998) using curve fitting

of experimental data. We slightly modified those expressions to take into account the contribution of resin cure to the change of elastic properties of the fiber mat (Appendix 1).

It is assumed that the mass of oven-dry fiber material in each grid element is constant (Thömen 2000; Thömen and Humphrey 2006). Actually, the volume of each element changes with time as a consequence of mat compression. Thus, the calculated oven-dry vertical density profile changes with time.

Wang and Winistorfer (2000a, 2000b), Winistorfer et al (2000), Wang et al (2001a, 2001b, 2004), and Thömen and Ruf (2008) demonstrated the impact of the pressing schedule on vertical density profile development. In our numerical study, tests were conducted for different press closing schedules. However, because only one pressing schedule was used to perform our laboratory experiments, validation of numerical results was only possible in this case. Press opening (venting period) was not modeled. The pressing cycle considered in our numerical study had a total duration of 268 s.

Moving Domain and Material Derivative

Mathematical concepts introduced in this section are presented in more detail in Garrigues (2007). Because the fiber mat is compressed and changes shape, it can be considered a moving domain. Oven-dry mass of the mat remains constant with time. However, mat density changes because its volume changes. To capture the compression of the mat, all calculations were performed on a moving geometry. Calculation of the displacement field over the domain allows one to keep track of each material particle movement.

To each material particle p of a moving domain, one can associate different physical quantities G such as scalar functions (temperature, moisture content, pressure), vectors (displacement, velocity), or tensors (thermal conductivity, strain). Material (particular) derivative of G is defined as time derivative of G when following a particle p of the material domain in its movement.

Assume that G is a function of an independent variable t and of three real-valued functions f, g, h , which are also associated with p and depend on t . Thus, if x represents the position of particle p at time t , one can write $G(x, t) = G(t, f(x, t), g(x, t), h(x, t))$. The chain rule applies and the material derivative of G associated with a material particle p is given by

$$\frac{DG}{Dt} = \frac{\partial G(t)}{\partial t} + \frac{\partial G}{\partial f} \frac{Df(x, t)}{Dt} + \frac{\partial G}{\partial g} \frac{Dg(x, t)}{Dt} + \frac{\partial G}{\partial h} \frac{Dh(x, t)}{Dt} \quad (1)$$

Because particle p is followed in its movement, assume that it occupies position x_1 at time t_1 and position x_2 at time t_2 with $t_2 = t_1 + \Delta t$. Then, each time derivative on the right side is regarded as a limit (with fixed particle p); for instance,

$$\frac{Df(x, t)}{Dt} = \lim_{\Delta t \rightarrow 0} \frac{f(x_2, t_1 + \Delta t) - f(x_1, t_1)}{\Delta t} \quad (2)$$

From the numerical standpoint, a finite difference scheme is used to discretize and approximate time derivatives such as the one presented in Eq 2. Displacement of a particle p is calculated at each time step by the mechanical model, and its position is updated. No material particles move in or out of the material domain. The same conservation principles of physical quantities associated with material particles of a moving domain apply as those presented in Part 1 of this study and in Kavazović (2011).

Mechanical Model

The governing equation for the mechanical model is expressed in terms of time- and space-dependent displacement field $U(x, t)$. Compression of the mat obeys Newton's second law:

$$\rho_{MAT} \frac{Dv}{Dt} - \text{div}(\sigma(U)) = 0 \quad \text{in } \Omega(t) \quad (3)$$

where ρ_{MAT} is the mat's wet density, v the velocity field, σ the second-order stress tensor (Appendix 1), and $\Omega(t)$ represents the evolving computational domain (fiber mat). In Eq 3, the inertial term ($\rho_{MAT} \frac{Dv}{Dt}$) is considered negligible during

the hot pressing process and will not be taken into account in further discussions.

Constitutive law. To establish a constitutive law relating U to σ , the following considerations were taken into account. The phenomenon of material aging was considered at the macro level. Aging is defined as the time dependency of the material properties. Because wood and wood-based composites are hygroscopic materials, aging is induced by variable moisture content and temperature conditions. This is taken into account by considering rheological properties as functions of evolving M and T ; hence material properties vary in time. Therefore, variations in M and T are directly linked to softening and hardening of wood. An increase in M and T in solid wood generates swelling, whereas a decrease causes shrinkage. In this study on MDF hot pressing, as a first approach, swelling and shrinkage were not taken into account.

We used Hooke's law as a constitutive law:

$$\dot{\sigma} = E: \dot{\varepsilon} + \dot{E}: \varepsilon \quad (4)$$

where σ is a second-order Cauchy stress tensor, E is a fourth-order elasticity tensor, and $\varepsilon(U) = \frac{1}{2} [\nabla U + (\nabla U)^T]$ is the second-order strain tensor. The different coefficients of E and their dependency on temperature, moisture content, and resin cure degree are described in Appendix 1.

We also tested an approach proposed by Dubois et al (2005) with a rheological model satisfying the second principle of thermodynamics (positive dissipation hypothesis). In our aging linear elasticity model, two distinct constitutive laws were used to comply with thermodynamic requirements: Hooke's law for softening (sorption) and a tangent law defined by Bazant (1979) for hardening (desorption) behavior. No differences in results occurred with respect to the simple model of Eq 4.

Incremental formulation. Eq 2 suggests that the time derivatives of ε and σ can be approximated

(Ghazlan et al 1995; Dubois et al 2005; Beuth et al 2008) by

$$\frac{D\varepsilon}{Dt} \approx \frac{\Delta\varepsilon}{\Delta t} \quad ; \quad \frac{D\sigma}{Dt} \approx \frac{\Delta\sigma}{\Delta t} \quad (5)$$

where $\Delta\varepsilon$ and $\Delta\sigma$ are instantaneous increments of strain and stress, respectively. With $N = 0, 1, 2, \dots$ and $t_0 = 0$, we denote time increment $\Delta t = t_{N+1} - t_N$, $\Omega_N = \Omega(t_N)$, $E_N = E(t_N)$, $\varepsilon_N = \varepsilon(t_N)$ with the time variation of E defined as $\Delta E = E_{N+1} - E_N$. The composite constitutive law for aging linear elastic material behavior (Eq 4) now reads

$$\Delta\sigma = E_{N+1} : \Delta\varepsilon + \Delta E : \varepsilon_N \quad (6)$$

It is usually assumed that the inertial component is negligible (ie $\rho_{MAT} \frac{Dv}{Dt} \approx 0$), and the problem is regarded as quasistatic (Ghazlan et al 1995; Beuth et al 2008): at each time step, static equilibrium is assumed (quasistatic assumption). The time evolution of mat geometry is simulated by imposing successive load increments on the mat. Compression is regarded as a step-by-step process evolving by time increment Δt . Development of strain and stress is then regarded as an incremental process:

$$\varepsilon_{N+1} = \varepsilon_N + \Delta\varepsilon; \quad \sigma_{N+1} = \sigma_N + \Delta\sigma \quad (7)$$

with ε_N and σ_N representing actual accumulated strain and stress, respectively, whereas ε_{N+1} and σ_{N+1} represent their values at the end of the next load increment. This allows retaining accumulated strain and stress history within storage variables ε_N and σ_N .

With these assumptions and Eq 6, Eq 3 is written in incremental formulation as follows:

$$\begin{aligned} -\text{div}[\Delta\sigma] &= \text{div}(\sigma_N) \quad \text{i.e.} \quad -\text{div}[E_{N+1} : \Delta\varepsilon + (\Delta E) : \varepsilon_N] = \text{div}(\sigma_N) \\ & \hspace{20em} \text{in } \Omega_N \\ U_{N+1} &= U_N + \Delta U \quad \text{with} \quad \Delta\varepsilon = \varepsilon(\Delta U) = \frac{1}{2} \left[\nabla(\Delta U) + (\nabla(\Delta U))^T \right] \end{aligned} \quad (8)$$

Eq 8 is thus written in terms of unknown displacement increment ΔU and is discretized by the finite element method. Appropriate boundary conditions are subsequently specified.

Computational Domain

Our mathematical model is written in a general 3D form, and our code can perform simulations on 2D and 3D geometries (Fig 1a). The effect of a daylight delay (the time necessary for the top platen to touch the mat) (Lee et al 2007) was ignored, and geometric symmetry was assumed (Carvalho and Costa 1998; Carvalho et al 2001, 2003; Nigro and Storti 2001; Thömen and Humphrey 2003, 2006; Dai and Yu 2004; Pereira et al 2006; Yu et al 2007). In 3D, there are three planes of symmetry (Fig 1b): a horizontal mid-plane and two vertical midplanes. Therefore, our computational domain represents one-eighth of the full 3D geometry or one-fourth of the full 2D geometry when calculations are performed in 2D. The domain considered for calculation was meshed with a nonuniform $24 \times 24 \times 20$ grid whose hexahedral elements were concentrated toward external planes (surface and exterior edges). The concentration of elements was created by a geometric progression with a common ratio of 0.9. We work on a moving domain (Fig 1b-c): 280 mm (half length in x direction) by 230 mm (half width in y direction) by half mat transient thickness (half thickness in z direction starting at 91 mm at the beginning of pressing and ending at 6.5 mm). Clearly, mat thickness evolves during pressing, and Fig 1c shows deformation of computational domain at different moments in time as a result of press closing. The mat is also free to expand in the x and y directions.

Density Profile and Mat Compression

During the mat compression process, total oven-dry mass of fiber material does not change.

However, material and rheological properties of the mat, such as local density, porosity, permeability, and thermal conductivity, evolve in time and space. Generally, the vertical density

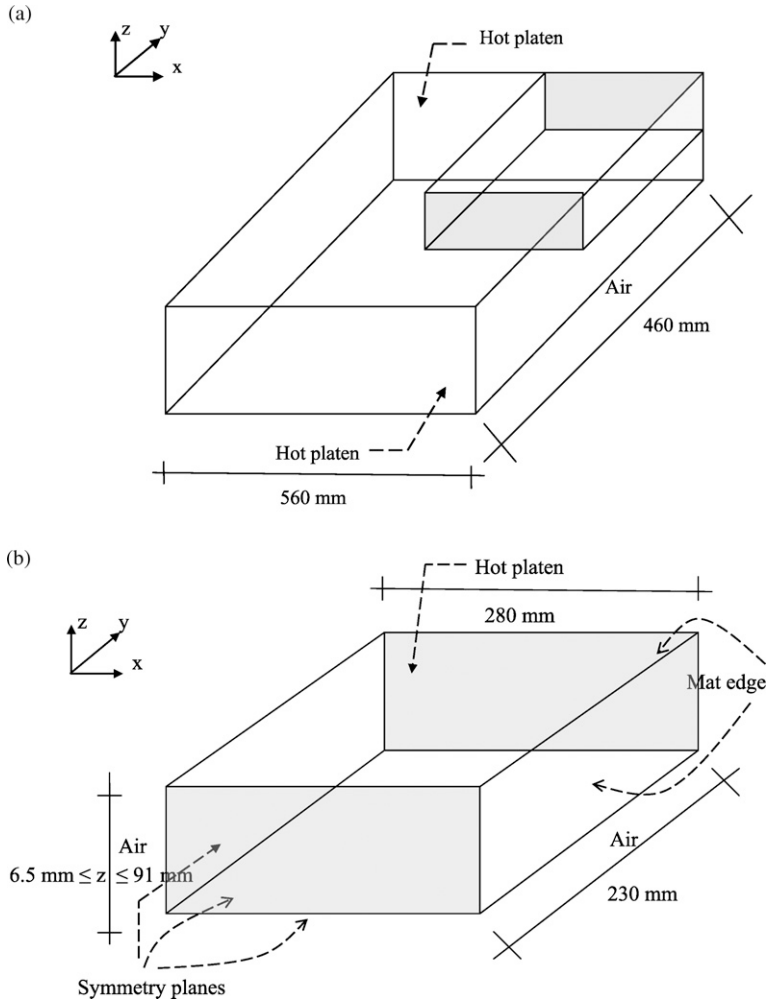


Figure 1. (a) Full 3D geometry of a fiber mat; (b) computational domain in 3D (one-eighth of the full geometry); (c) evolving 3D computational domain at different moments in time (one-eighth of the full geometry: $0 < x <= 280$ mm, $0 < y <= 230$ mm).

profile of compressed composite panels is not uniform. It mainly exhibits a characteristic M shape with higher density in the surface layers and lower density in the core (Carvalho et al 2001, 2003; Wang et al 2001a, 2001b; Thömen and Ruf 2008). It is regularly observed that the transition region from low to high density is rather thin (Carvalho et al 2001, 2003; Wang et al 2001a, 2001b). This nonuniform densification is attributed to variations of T and M and interactions among heat and moisture transfer

phenomena, glass transition of lignin and hemicelluloses, and mechanical compression of the mat (Wolcott et al 1990; Kamke and Wolcott 1991; Dai and Yu 2004; Thömen and Ruf 2008). In general, the mat becomes softer and easier to compress when temperature or moisture content increases (Kamke and Wolcott 1991; von Haas and Frühwald 2000).

In this study, the evolution of a nonhomogeneous oven-dry vertical density profile of the

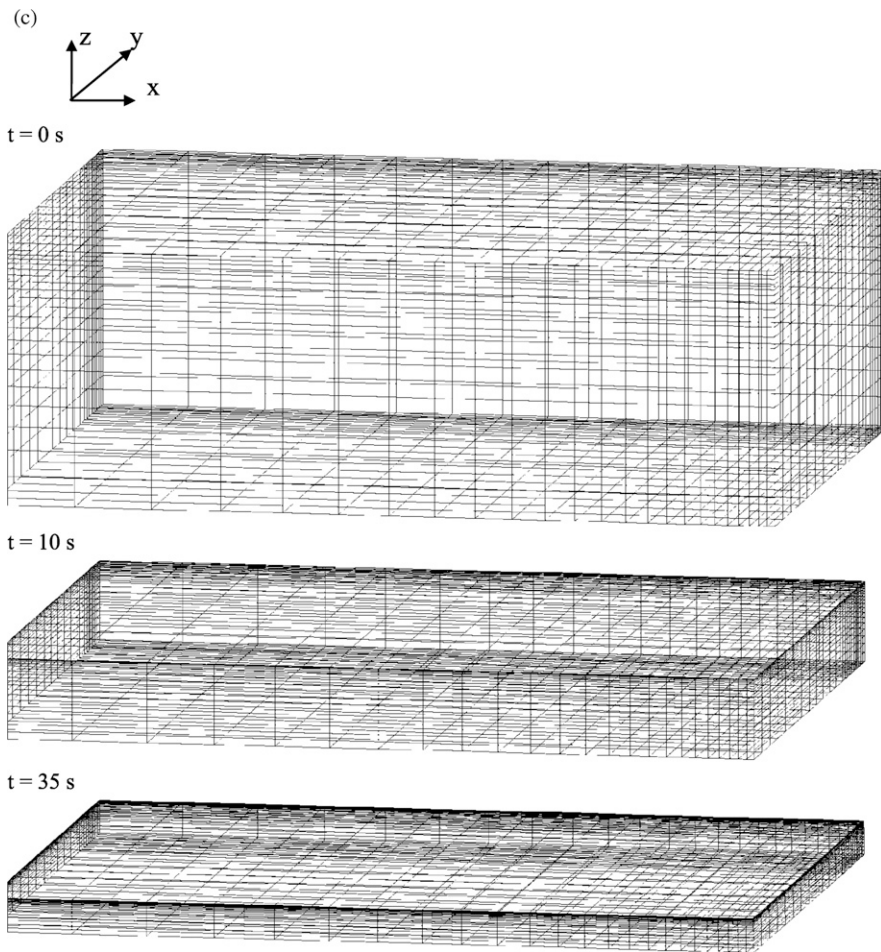


Figure 1. Continued.

mat during hot pressing was calculated by a mechanical model for an aging elastic material. Mat thickness decreased as a function of the press closing schedule (Figs 1c and 2a) of a Dieffenbacher (Eppingen, Germany) laboratory batch press. The pressing schedule of 268 s was divided into five steps. The initial mat thickness of about 182 mm was decreased to 37 mm in the first 15 s (Step 1). The press remained in this position for the next 10 s (Step 2) followed by the second compression, which decreased mat thickness to 19 mm at 42 s (Step 3). A slow compression phase lasting 120 s followed at the end of which the mat reached its final thickness of 13 mm (Step 4) at 162 s. The hot platens

remained in this position (Step 5) until 268 s. The curve-presenting evolution of mat thickness with time can be seen in Fig 2a. The venting period was not modeled and therefore is not presented.

From the numerical simulation standpoint, the densification process can be described as follows: at each time step, an increment of the platen displacement is imposed as a Dirichlet boundary condition at the surface in contact with the top platen. As a reaction to this solicitation, the mechanical model calculates the corresponding displacement of each mesh node and mat geometry is updated accordingly. Because

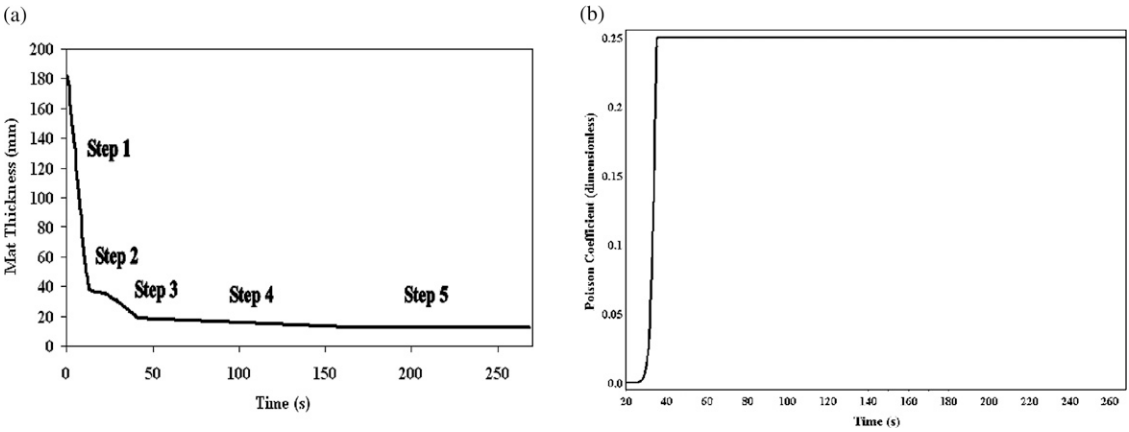


Figure 2. (a) evolution of mat thickness with time. Venting period is not modeled and therefore is not presented; (b) evolution of Poisson's coefficient.

oven-dry mass of the material remains constant within each element, the oven-dry density evolves because of the change in volume of each element. Because mat porosity is a function of oven-dry density, it is thus time- and space-dependent. Mat porosity is calculated by the following equation:

$$\Phi = 1.1 \times \left(1 - \frac{\rho_{OD}}{1530} \right) \quad (9)$$

where a correction factor for MDF mats determined by Belley (2009) multiplies the expression proposed by Siau (1984) for solid wood. Heat and mass transfer properties of the fiber mat, such as thermal conductivity and specific gas permeability, were presented in Part 1.

Initial and Boundary Conditions

Appropriate initial and boundary conditions for the heat and mass transfer model were described in Part 1 of this study. We shall now consider initial and boundary conditions for the mechanical model.

At the beginning of pressing ($t = t_0 = 0$), the mat is assumed at rest and stress-free and the displacement field is assumed null. This is expressed by the following initial conditions:

$$U(0) = U_0 = \vec{0} \quad \text{and} \quad \sigma(0) = \sigma_0 = 0 \quad (10)$$

To mimic press closing (Fig 2a), at each time step, an increment of displacement field (ΔU) is

imposed at the top surface in the z direction by a Dirichlet boundary condition (ΔU_Z is deduced from the evolution of the mat thickness; Fig 2a). No movement in the x - y plane is allowed at the top surface ($\Delta U_X = \Delta U_Y = 0$). Because we take advantage of symmetry, the working domain represents one-eighth of the mat (Figs 1a-b) and boundary conditions have to be imposed on the three symmetry planes. The symmetry plane $z = 0$ is not allowed to move in the z direction ($\Delta U_Z = 0$). The symmetry plane $x = 0$ does not move in the x direction ($\Delta U_X = 0$), whereas $y = 0$ does not move in the y direction ($\Delta U_Y = 0$). However, they both compress in the z direction following the movement of the closing press platen (Fig 1c). The exterior faces $x = 280$ mm and $y = 230$ mm follow the press closing movement in the z direction and are both free to expand in the x and y directions (zero traction, $\sigma \cdot \vec{n} = 0$, \vec{n} is outward unit normal).

Numerical Coupling of Mechanical and Heat and Mass Transfer Models

At each time step, the coupled heat and mass transfer model is solved first. The three non-linear conservation equations for heat and mass transfer form a fully coupled system and are solved together. This system is discretized in space by the finite element method using Q1 finite elements (Bathe 1982; Reddy 2006)

and is solved by means of Newton's method (Kavazović *et al.* 2010). All material properties are updated at each nonlinear iteration, except for the oven-dry density profile, which remains unchanged at this stage. Once the convergence criterion is reached, the program provides new values for the three state variables P_a , P_v , and T from which we calculate M . Those updated variables are then used as input to the mechanical model. Indeed, as they appear in expressions of the aging elasticity tensor coefficients, those new values will update the rheological parameters of the mat and be used in calculations of mat compression. The increment of the press platen position is imposed (Dirichlet boundary condition) at the top surface of the mat. The displacement vector field is then obtained as a solution of the mechanical model, which is discretized in space by the finite element method using Q2 finite elements (Bathe 1982; Reddy 2006). The position of each grid point is then updated by the corresponding increment of displacement vector (ΔU). As the grid points move, the volume of each element eventually changes. Consequently, the value of oven-dry density of each element changes too. The new oven-dry density field is then used to update the mat heat and mass transfer properties. Hence, we are ready to undertake calculations with the heat and mass transfer model at the next time step. Details on how the implicit second-order two-step backward differentiation formula was applied as a time discretization scheme can be found in Kavazović (2011).

RESULTS AND DISCUSSION

To perform successful numerical simulations, coefficients and expressions for different material properties are needed. For example, we proposed a formula to account for extent of resin cure on MOE (Eq 13 in Appendix 1). More research is also needed on Poisson's ratio of the mat during early stages of compression. Indeed, at the beginning of pressing, the mat is a loose material. It eventually gains more cohesion as pressing progresses. To reflect this transition, an appropriate formula for Poisson's coefficient is needed, especially in the early stages of pressing.

We attempted to address that issue by proposing a sigmoid shape function allowing for a smooth transition from a loose stage to a more cohesive material (Fig 2b and Eq 14 in Appendix 1). Experimental data are needed to validate our hypothesis and have a better understanding of this phenomenon.

Coupling of mechanical and heat and mass transfer 3D models allowed for dynamically predicting development of the vertical density profile as a function of the pressing schedule. Figure 3a shows numerical predictions of the vertical density profile in the panel centerline. At the early stage, average density rapidly increased and the vertical density profile appeared uniform throughout the thickness. About 15 s after the beginning of compression, a steep density gradient developed close to the surfaces. As press closure progressed, average density of the mat increased, whereas mat thickness decreased. Figure 3a shows the development of a U-shaped profile with a high-density region near the press platens, a significantly lower density in the core, and a transition region in between. Panels pressed in the laboratory presented an M-shaped profile, mostly because of resin precure at the surfaces in contact with the hot platens. The model was not able to reproduce the M-shaped profile, probably because of improper capture of the impact of resin cure on mat mechanical properties. Results obtained at four representative locations in the symmetry width–thickness midplane of a 3D geometry illustrate numerical predictions of the evolution of oven-dry (Fig 3b) and wet densities (Fig 3c), respectively. As expected, density of the surface layer increased faster than elsewhere. During Step 5 (Fig 2a), the press platens remained at the same position. Hence, a zero displacement increment was imposed and the oven-dry density profile remained unchanged (Fig 3b). This was expected because we were modeling linear elastic behavior. There is a qualitative similarity between our results and those presented by Wang *et al.* (2001a, 2001b, 2004) for a similar pressing schedule.

Numerical results obtained with the 3D-coupled mechanical and heat and mass transfer models

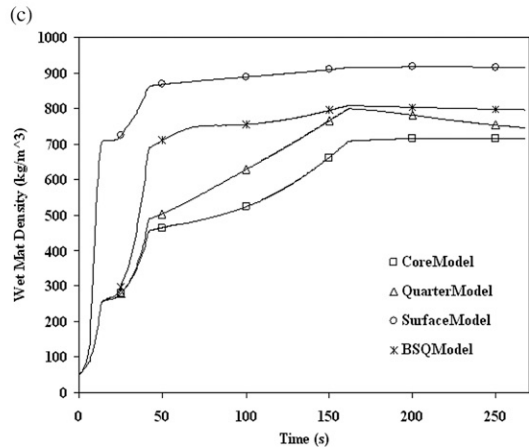
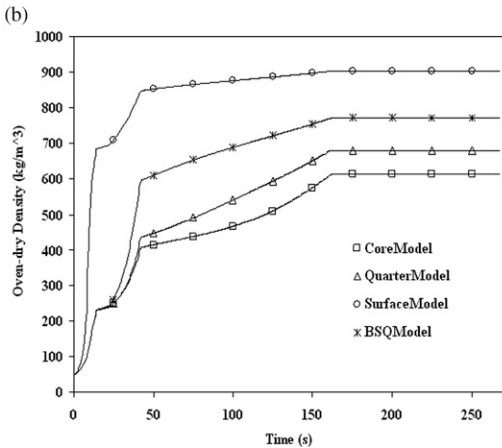
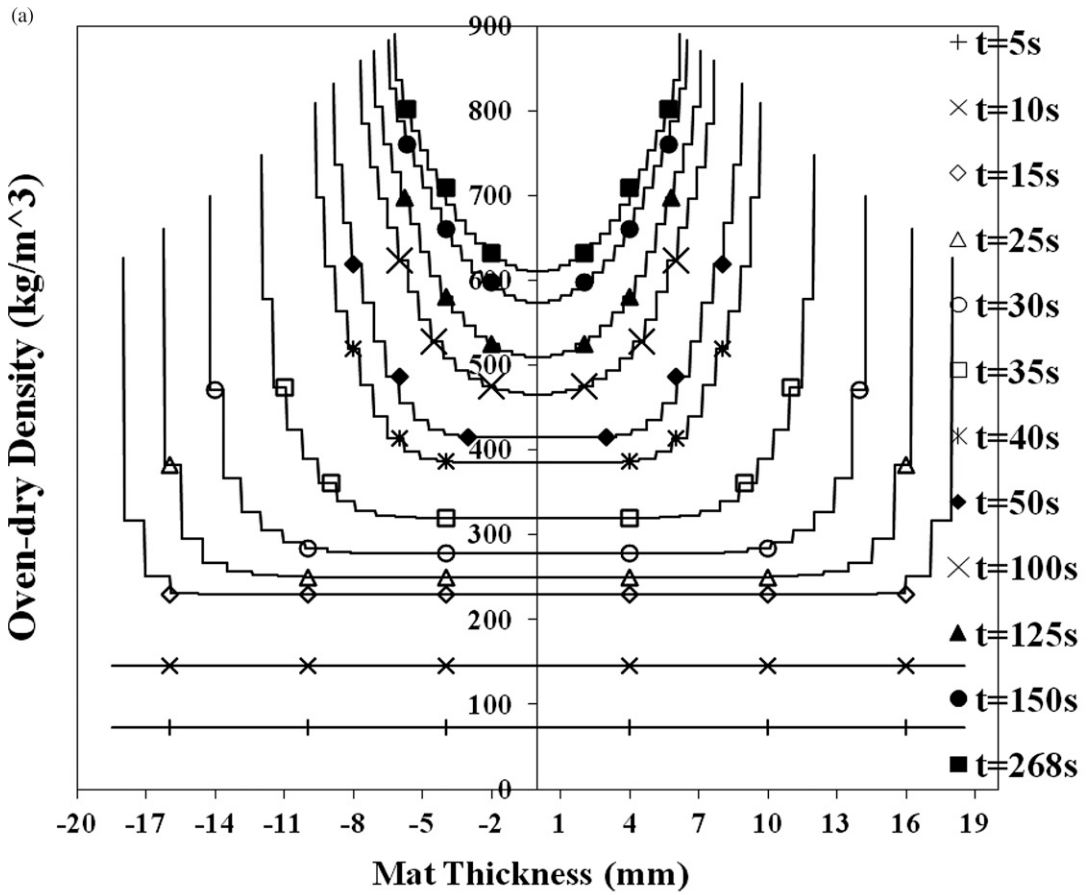


Figure 3. Results obtained with our 3D global model: (a) evolution of space- and time-dependent numerically predicted oven-dry vertical density profile; (b) predicted oven-dry density profile, values at four points in the vertical centerline; (c) bulk density profile at four points in the vertical centerline calculated by $\rho_{Mat} = \rho_{OD} (1 + M)$. (In all figures, special symbols such as \square , \circ , $*$, \diamond , ∇ are used to identify the different curves and do not represent experimental data unless the contrary is explicitly indicated.

exhibit good overall agreement with experimental measurements. Figures 4a-b present laboratory temperature and gas pressure measurements, respectively, together with numerically predicted results. In Fig 4a, the curve labeled *SurfaceLab* is the mean temperature measured in the laboratory at the surface in contact with the hot platen. That curve was imposed as a Dirichlet boundary condition for T at the surface. The curves labeled *CoreModel* and *QuarterModel* were obtained by numerical simulation and represent temperature at the center and at one-fourth of the thickness, respectively. As Fig 4a-b shows, numerically predicted temperature at the core and at one-fourth of the mat thickness in the vertical center plane closely follows evolution of in situ measurements. In particular, plateau temperatures and time when they were reached are similar. Numerical results underestimated average temperature curves. Maximum discrepancy from the measured average core temperature was approximately 4% (Fig 4a), and at one-fourth of the thickness, temperature was underestimated by up to 8% (Fig 4a).

In Fig 4b, numerical predictions of total gas pressure (P) at the core and surface locations are compared with experimental data. Large standard deviation bars, especially in the second half of pressing, reveal significant variations of gas pres-

sure in the laboratory measurements (Fig 4b). Maximum coefficient of variation was approximately 6%. Numerical results did not exhibit any vertical gradient in total gas pressure predictions. Thus, the curves of predicted P at the surface and at the core superimpose (curve labeled *Surface&CoreModel*) and are identified by the same symbol in Fig 4b. From the qualitative standpoint, the time evolution of gas pressure was well captured by the model. However, numerical results overestimate mean value of gas pressure experimental measurements by 10% in the case of pressure at the surface and by 15% at the core (Fig 4b). Nevertheless, compared with other numerical results in the literature (Zombori et al 2004; Pereira et al 2006; Thömen and Humphrey 2006), results obtained in this study are of similar quality.

When examining numerical results, the absence of total gas pressure gradient in the vertical center plane should be noticed. The same phenomenon is observed in most of the publications presenting numerically predicted total gas pressure (Carvalho and Costa 1998; Carvalho et al 2003; Zombori et al 2003; Pereira et al 2006; Thömen and Humphrey 2006; Yu et al 2007). Measurements of cross-sectional gas pressure reported by Thömen (2000) for MDF mats

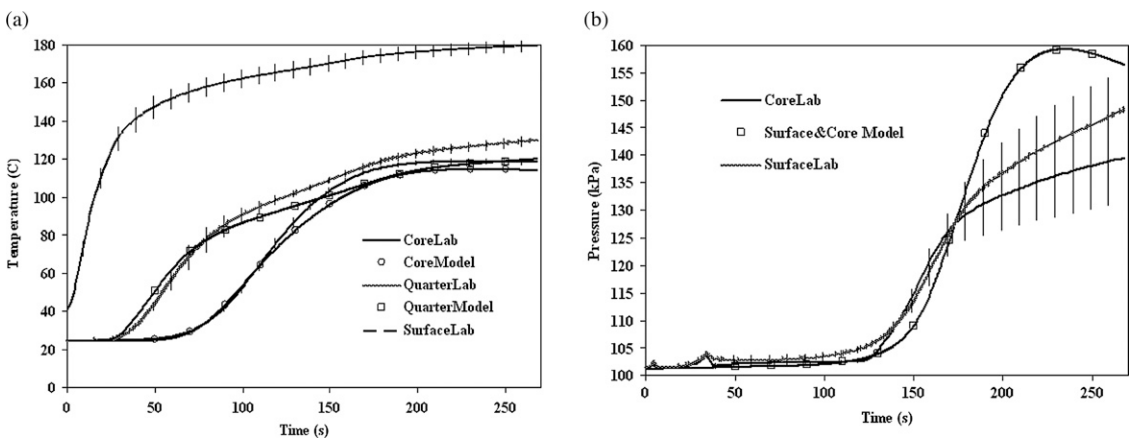


Figure 4. Numerical results obtained. (a) temperature evolution in time: measurements at surface, core, and one-fourth of the thickness and numerically predicted results at the core and one-fourth of the thickness; (b) total gas pressure evolution in time: experimental and numerical results at surface and core. Curve labeled *Surface&CoreModel* was obtained by numerical simulation, and the two others are experimental results. Vertical bars represent standard deviation from the mean value.

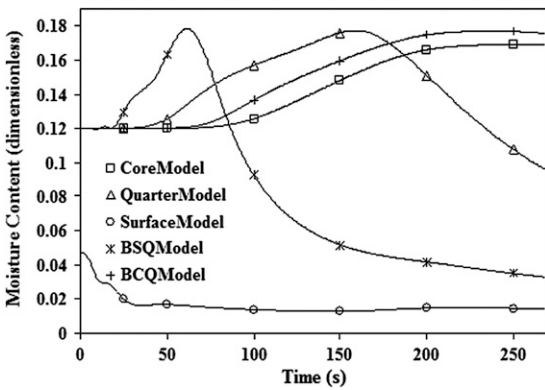


Figure 5. Numerical predictions of moisture content (MC) evolution at five equidistant points in the vertical centerline (BSQ, between surface and quarter; BCQ, between center and quarter).

validate these numerical results. Nevertheless, we and the previously mentioned authors observed the development of a significant horizontal total gas pressure gradient, especially in the central plane, which drives the gas out of the mat.

Figure 5 shows the evolution of predicted mat moisture content (M) at the core, at one-fourth of the thickness, at the surface, and at the mid-points between the core and one-fourth of the thickness as well as between the surface and one-fourth of the thickness. As expected, moisture content near the press platen drops rapidly and remains low. The curves of Fig 5 clearly

illustrate movement of bound water from the hot surface toward the cooler core region. These results are in accordance with Yu et al (2007).

Figure 6 summarizes the results for partial air (P_a) and vapor (P_v) pressures. Figure 6a shows that, at the beginning of pressing, air pressure rapidly dropped in the surface layers, whereas it remained almost stable in interior layers. At the same time, because of the evaporation process taking place close to the hot surface, vapor pressure exhibited the opposite behavior: it increased at the surface and remained low elsewhere (Fig 6b). This created vertical (cross-sectional) partial air and vapor pressure gradients. Because total gas pressure remained almost constant during the first half of the pressing (Fig 4b), it can be concluded that the increase in P_v was proportional to the decrease in P_a . Hence, water vapor replaced air and became the main component of the gaseous phase. Development of vertical P_a and P_v gradients is clearly visible in Fig 6. Those gradients drive the molecular diffusion of air and water vapor within the gas phase. Furthermore, because surface temperature increased rapidly, evaporation of bound water was intense in regions close to hot platens. As a result, M at the surface decreased and local vapor pressure increased. As seen in Fig 6b, a steep P_v gradient developed. This facilitated the molecular diffusion of the vapor within the gas phase

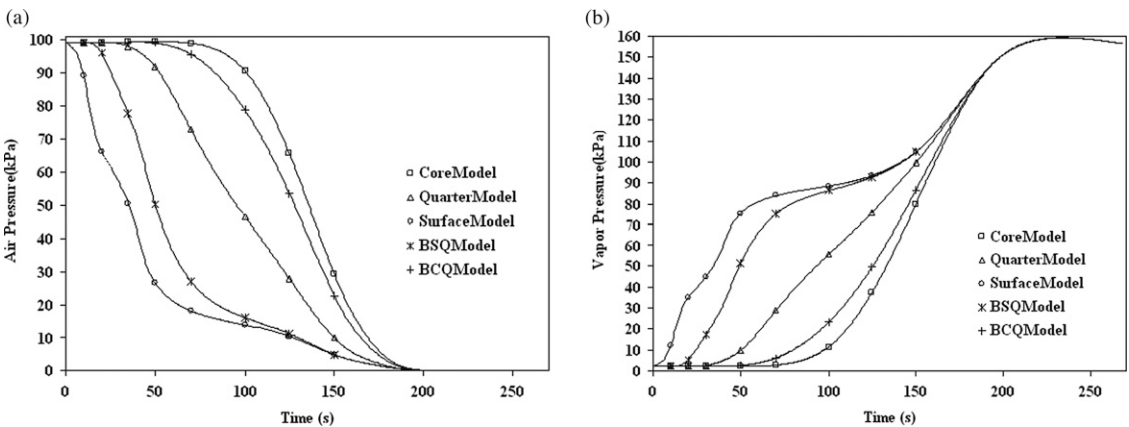


Figure 6. Numerical predictions of partial air and vapor pressure at five equidistant points in the vertical centerline (BSQ, between surface and quarter; BCQ, between center and quarter). Evolution of (a) partial air pressure and (b) partial vapor pressure.

toward the core. Given that the core had a lower temperature, water vapor condensed and thus increased the local moisture content (Yu et al 2007). Consequently, the amount of bound water present in the core region of the mat increased with time (Fig 5). It takes large amounts of energy to evaporate the accumulated bound water. That explains the temperature plateau in the core (Fig 4a). At $t = 160$ s, Fig 6 suggests that almost all the air was replaced by water vapor in the gas phase. Also, the vertical partial air and vapor pressure gradients vanished (Fig 6). Total gas pressure started to increase significantly (Fig 4b), and a temperature plateau was set at the core (Fig 4a). This suggests that an intense phase change of water in the core layer began (Fig 5). Also, as densification continued, gas permeability of the mat decreased and contributed to gas pressure build-up, especially in the core layer. That difference in gas pressure between the core and the edges resulted in gas flow in the panel's horizontal plane, which became the predominant direction of mass transfer. This is in agreement with observations made by Yu et al (2007).

Numerical Tests

Our goal was to develop a robust numerical tool able to provide reliable numerical results under different pressing conditions. After validation of the numerical results presented previously, the model was used to perform several tests. For each time step, the workload was distributed as follows: one-third of the time for the heat and mass transfer problem (Newton's method converged in four or five iterations) and two-thirds for the mechanical model (conjugated gradient method preconditioned by successive overrelaxation). In our case, 3D computations were 5 to 10 times longer than 2D calculations. Because the number of tests to be performed was large, we decided to run them on 2D geometry.

2D versus 3D Predictions

When the calculations were performed on 2D instead of 3D geometry, one can expect some

changes in numerically predicted results. Details on impacts of the change from 3D to 2D can be found in Kavazović (2011). The 2D and 3D results were very similar during the first half of pressing, but some differences occurred in the second half, mainly in the plateau values of the variables. These differences were most likely caused by the small in-plane size of laboratory panels (0.56×0.46 m), which enhanced boundary effects (better venting in 3D). For instance, at the core, total gas pressure in 2D was 20% higher than in 3D. Also, in 2D, the plateau value for M increased by a maximum of 3%, whereas the increase of T was about 5%. However, oven-dry density predictions do not appear to be affected by the transfer from 3D to 2D geometry.

Convergence with Mesh

We verified that the solutions converge when the 2D mesh is refined. Numerical simulations were run using the laboratory pressing schedule with a time step of 0.1 s and the computational domain representing one-fourth of the mat. Calculations were performed on a series of uniform rectangular meshes with an increasing number of elements. We worked on the following 2D grids in which the first number stands for the amount of elements in the width (x) direction and the second number stands for the amount of elements in thickness (z): 16×16 , 32×16 , 64×32 , 128×64 , 256×128 . Convergence with an increasing number of elements was observed very quickly. Also, a study was conducted to determine the impact of the layout of elements in a finite element grid (Kavazović 2011). A nonuniform 2D mesh with 24 rectangular elements in the width direction and 20 elements in the thickness direction was created representing one-fourth of the mat. A geometric progression with the common ratio of 0.9 was used to concentrate the elements toward the boundaries (hot platen and exterior border). Results obtained with this grid were compared with those obtained with finer regular grids: 64×32 , 128×64 , 256×128 . Comparisons revealed very good agreement among the results, suggesting that a coarse grid with elements

concentrated in appropriate areas of the mat could adequately capture the evolution of physical phenomena.

Impact of Time Step Length

The impact of time step length on results was also examined for the laboratory pressing schedule. Tests were performed on two 2D grids (32×16 and 64×32) with different time steps: 0.025, 0.05, 0.1, 0.2, 0.4, and 0.5 s. We used an implicit second-order backward finite difference scheme for time discretization. This study revealed that the solutions converge with a decrease of time step and that it had very little impact on the solutions. This suggests that the combination of finite element method and implicit second-order backward finite difference scheme allows one to use larger time steps without losing accuracy. In our numerical simulations, a time step of 0.5 s was often used in 3D and time steps of 0.1 and 0.5 s in 2D.

Pressing Schedules

Cold pressing tests (platens at $T = 25^\circ\text{C}$) were performed with a 64×32 grid for different pressing schedules with a time step of 0.5 s. Because the temperature of the platens was equal to ambient temperature, there was neither heat nor mass transfer. However, the closing

press platens induced mat densification with time. Numerical results for cold pressing systematically produced flat vertical density profiles. This was the expected behavior in these conditions.

Robustness and flexibility of the global model were tested in different pressing situations. Numerical simulations were carried out for seven different pressing schedules on several grids. However, we only present some of the results obtained with a 64×32 grid for a few pressing schedules with a time step of 0.1 s.

Figure 7 shows four different pressing schedules. The press closing dynamics from our laboratory experiments were used as reference for qualitative comparisons with three other pressing schedules: one-, two-, and four-step pressing schedules, respectively (Fig 7). All pressing schedules were simulated across a period of 268 s.

One-step closure simulated a rapid compression in which the mat reached a final thickness of 13 mm after 20 s. The press platens remained at the final position until the end (Fig 7; curve identified as 1 Step). For this one-step closure, the time of first compaction was estimated at 18.6 s. We defined time of first compaction as the moment when the mat reached 1.9 times its final thickness. This parameter was used in our definition for time evolution of Poisson's ratio (Appendix 1, Eqs 14 and 15). The time of first compaction was estimated at 71 s for the two-step

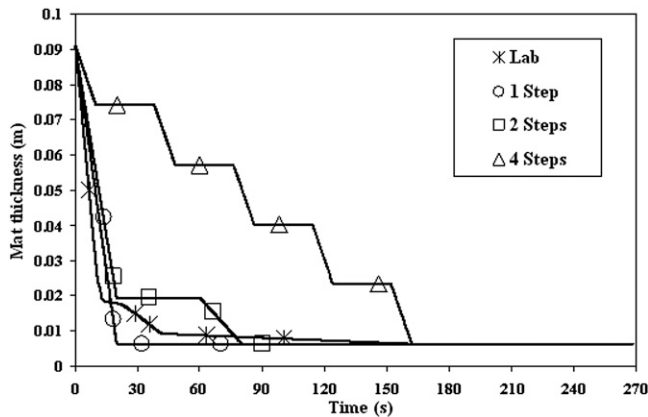


Figure 7. Evolution of mat thickness as a function of four different pressing schedules.

pressing schedule and 158.5 s for the four-step schedule.

Typical tendencies at the core for oven-dry density, temperature, moisture content, and total gas pressure fields are presented in Fig 8. One-step closure densified the core region the most rapidly (Fig 8a), hence increasing thermal conductivity, which resulted in somewhat faster increase of the core temperature (Fig 8b). The higher temperature accelerated the moisture evaporation process in the core region (Fig 8c). As a result, a slightly higher gas pressure was produced in the core region in early stages of pressing (Fig 8d). Figure 8c suggests that final moisture content in the core region was lower when the one-step press closure was applied. Nevertheless, final gas pressure did not appear to be higher than the one

obtained when the laboratory pressing schedule was simulated (Fig 8d).

Two-step and laboratory press closing programs had the same characteristics and resulted in similar evolution of temperature, moisture content, and total gas pressure fields in the core (Fig 8b-d). However, oven-dry densities (Fig 8a) exhibited a different behavior. Indeed, because a linear elastic mechanical model was used, the development of oven-dry density was heavily influenced by press closing dynamics.

The four-step closing schedule compressed the mat slowly, causing moderate densification of the core (Fig 8a). This adversely affected thermal conductivity increase. Therefore, noticeable delays occurred in temperature evolution

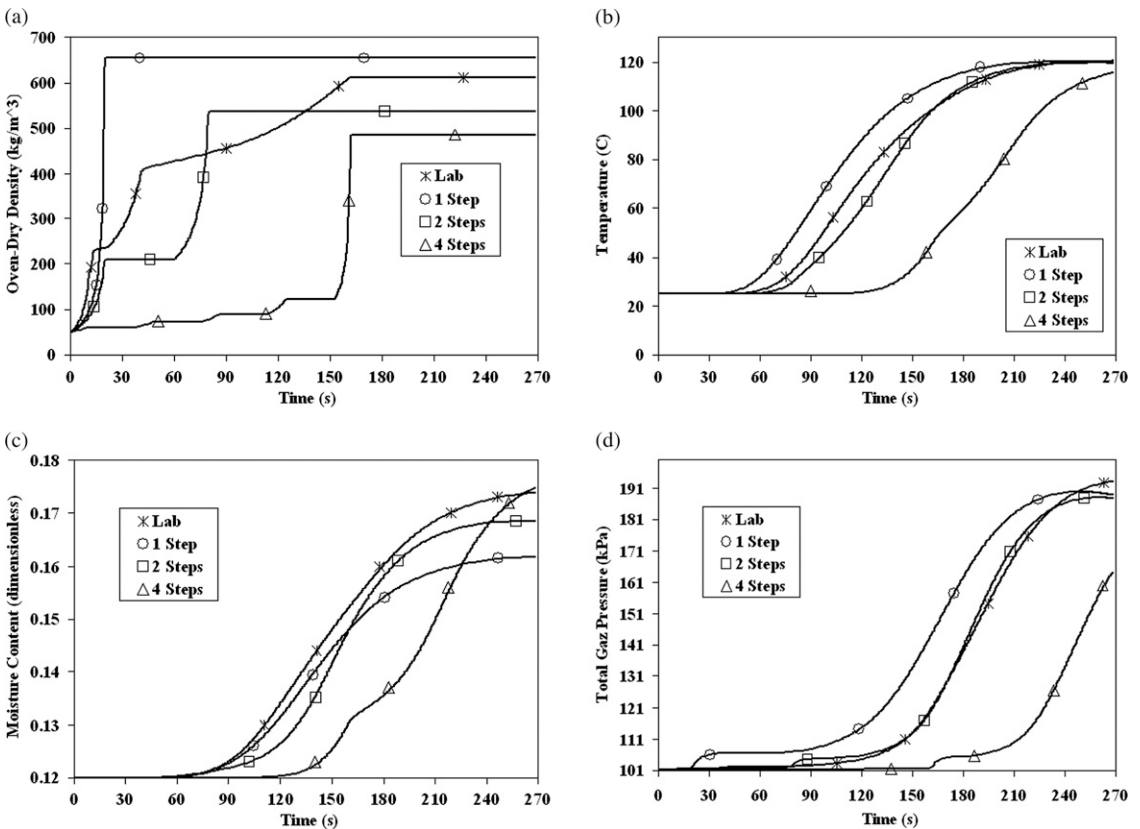


Figure 8. Effect of four different pressing schedules on evolution of 2D numerical results at the core location for (a) oven-dry density, (b) temperature, (c) moisture content (MC), and (d) total gas pressure.

(Fig 8b) when the four-step closing was applied. This eventually slowed down mass transfer toward the core (Fig 8c). As a result, phase change started later than for the other pressing scenarios. Also, a low core density resulted in higher gas permeability. Thus, when all these factors were combined, significant delays occurred in pressure build-up when the slow four-step schedule was simulated (Fig 8d).

Evolution of 2D Profiles

Figure 9 depicts evolution of 2D profiles of T , M , and P_v . Results are presented on one-half of a 2D geometry in which full thickness and a half width were considered. Top and bottom hot platens compressed the mat from the left and right sides, respectively. Therefore, thickness is represented by the smaller sides of the rectangle. The

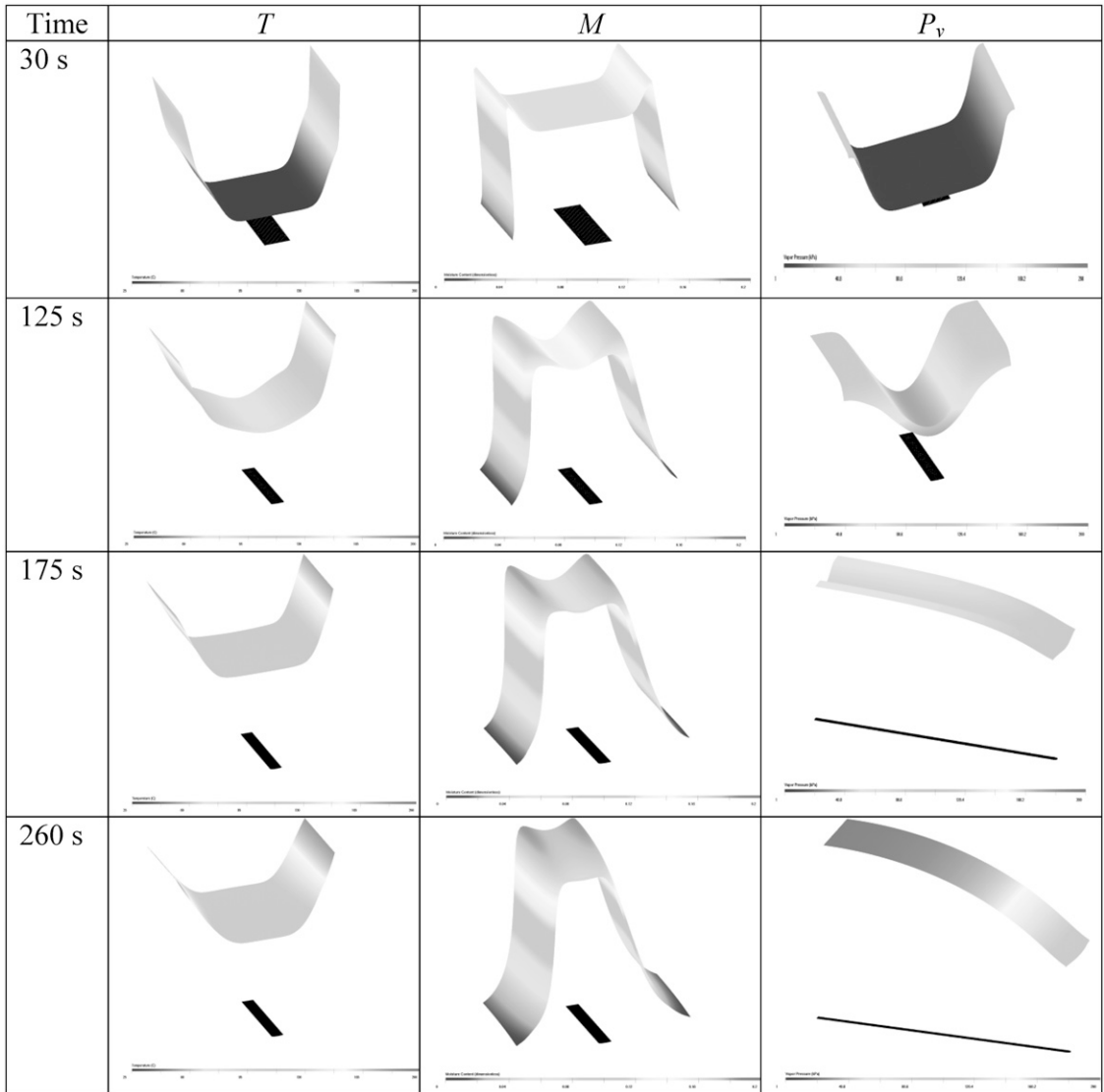


Figure 9. Evolution of 2D profiles for temperature, moisture content (MC), and partial vapor pressure.

small side closer to the viewer is the boundary at which exchange with ambient air occurs. Hence, the symmetry (core) plane is represented by the small boundary located far back on the graph. All graphs in Fig 9 display computational domain meshed by a 256×128 element grid. Domain thickness decreased with time as press platens compressed the mat following our laboratory closing schedule. Nevertheless, for the sake of clarity, width of the displayed solution surfaces was kept constant with time.

A time step of 0.1 s was used in calculations, and numerically predicted results are presented at 30, 125, 175, and 260 s. Graphs of T , M , and P_v presented in Fig 9 show development of vertical gradients for the three variables. After 175 s, an interesting transition happened in the P_v field predictions (image was rotated 90° clockwise). Indeed, the P_v gradient across thickness appeared to vanish and a horizontal P_v gradient started to develop. At $t = 260$ s, the gradient across thickness completely disappeared and an in-plane horizontal gradient was well established, driving the gas phase out of the mat. At the same time, the temperature field still showed a gradient across thickness, whereas moisture content exhibited both a very pronounced gradient across thickness and a weak in-plane horizontal concentration gradient.

CONCLUSIONS

The main purpose of this study was to describe the methodology developed and solution strategy implemented to simulate MDF hot pressing on a moving domain. The proposed global model combined the finite element method with an implicit time scheme providing more flexibility in the choice of time step. An elastic constitutive law for aging material was used.

Results predicted by the global model for T and P exhibited good overall agreement with laboratory batch press experimental measurements. Temperature evolution and formation of characteristic temperature plateaus are well captured. Gas pressure gradient developed in the horizontal plane, whereas numerical results revealed the absence of the vertical gas pressure gradient in

the center plane. The model also produced valuable predictions for variables of interest that are difficult to measure in the laboratory such as evolution of density profile, partial air and vapor pressures, moisture content, RH, and degree of resin cure. During the first half of pressing, partial air and vapor pressure gradients were well developed in the cross-sectional direction. They vanished in the second half of pressing, and horizontal vapor pressure gradient developed.

The cross-sectional density profile played an important role in the evolution of rheological properties and inner conditions of the mat. Development of the vertical density profile was well predicted by our simple mechanical model, but improvements are required. A better knowledge of mat rheological properties is needed, especially at low-density values in the early stages of pressing to better capture the development of the density profile in the vicinity of the press platens and to consider the venting phase of the pressing cycle.

Local rheological mat conditions change in space and with time and are functions of mat density, temperature, moisture content, and adhesive cure. We considered the effect of adhesive cure on rheological mat characteristics. This proposed expression is only the first step in characterization of this complex relationship. A sensitivity study would be one way to investigate the relative importance and influence of resin cure on mat rheological properties and numerical results. Furthermore, the evolution of mat Poisson's ratio during the early stages of pressing definitely requires more investigation. We proposed an expression allowing for a smooth transition and increase of Poisson's ratio as a function of mat thickness. However, it would be interesting to further explore the correlation between Poisson's ratio and local density.

The present model provides reasonably reliable insight into complex dynamics of rheologic and heat and mass transfer phenomena occurring during hot pressing of fiber mats. It was tested under various pressing scenarios, and numerical results systematically showed reasonable tendencies. Our global model and finite element code proved to be robust tools to conduct further case studies.

Nomenclature

Partial nomenclature is presented here, whereas complementary information can be found in Nomenclature of Part 1 of this study.

<p>t = time [s] x = length [m] y = width [m] z = thickness [m] T = temperature field [K]; a state variable calculated by the model P_a = partial air pressure [Pa]; a state variable calculated by the model P_v = partial vapor pressure [Pa]; a state variable calculated by the model U = displacement field [m]; a state variable calculated by the model P = total gas pressure [Pa] M = moisture content [dimensionless] h = relative humidity [dimensionless] ρ_{OD} = oven-dry density of the mat [kg/m^3] Φ = porosity of the mat [dimensionless]</p>	<p>ρ_{MAT} = wet density of the mat [kg/m^3] α = resin cure degree [dimensionless] E_{el} = modulus of elasticity [Pa] E_X = modulus of elasticity in the x direction [Pa] E_Y = modulus of elasticity in the y direction [Pa] E_Z = modulus of elasticity in the z direction [Pa] G_{XY} = modulus of shear stress in the x-y plane [Pa] G_{YZ} = modulus of shear stress in the y-z plane [Pa] G_{XZ} = modulus of shear stress in the x-z plane [Pa] <i>Poisson</i> = Poisson's coefficient of compression [dimensionless]</p>
--	--

ACKNOWLEDGMENTS

We thank the Natural Sciences and Engineering Research Council of Canada (NSERC), FPIInnovations–Forintek Division, Uniboard Canada, and Boa-Franc for funding of this project under the NSERC Strategic Grants program. We also acknowledge Professor Patrick Perré for his comments and suggestions.

REFERENCES

- Bathe KJ (1982) Finite element procedures in engineering analysis. Prentice-Hall, New York, NY. 735 pp.
- Bazant ZP (1979) Thermodynamics of solidifying or melting viscoelastic material. *J Eng Mech Div* 105(EM6):933-955.
- Belley D (2009) Détermination des propriétés de transfert de chaleur et de masse des panneaux de fibres de bois MDF. MSc thesis, Université Laval, Québec, Canada. 70 pp.
- Beuth L, Benz T, Vermeer PA, Wieckowski Z (2008) Large deformation analysis using a quasi-static material point method. *J Theor Appl Mech* 38(1):45-60.
- Bolton AJ, Humphrey PE (1988) The hot pressing of dry-formed wood-based composites. Part I. A review of the literature identifying the primary physical process and the nature of their interaction. *Holzforschung* 42(6): 403-406.
- Bolton AJ, Humphrey PE, Kavvouras PK (1989) The hot pressing of dry-formed wood-based composites. Part VI. The importance of stresses in the pressed mattress and their relevance to the minimisation of pressing time and the variability of board properties. *Holzforschung* 43(6): 406-410.
- Carvalho LM, Costa CAV (1998) Modeling and simulation of the hot-pressing process in the production of medium density fiberboard (MDF). *Chem Eng Commun* 170:1-21.
- Carvalho LMH, Costa MRN, Costa CAV (2001) Modeling rheology in the hot-pressing of MDF: Comparison of mechanical models. *Wood Fiber Sci* 33(3):395-411.
- Carvalho LMH, Costa MRN, Costa CAV (2003) A global model for the hot-pressing of MDF. *Wood Sci Technol* 37:241-258.
- Dai C (2001) Viscoelasticity of wood composite mats during consolidation. *Wood Fiber Sci* 33(3):353-363.
- Dai C, Yu C (2004) Heat and mass transfer in wood composite panels during hot-pressing. Part 1. A physical-mathematical model. *Wood Fiber Sci* 36(4):585-597.
- Dubois F, Randriambololona H, Petit C (2005) Creep in wood under variable climate conditions: Numerical modeling and experiment validation. *Mech Time-Depend Mater* 9:173-202.
- Ganev S, Gendron G, Cloutier A, Beauregard R (2005) Mechanical properties of MDF as a function of density and moisture content. *Wood Fiber Sci* 37(2): 314-326.

- Garrigues J (2007) *Fondements de la mécanique des milieux continus*. Hermès-Lavoisier. Paris. 250 pp.
- Ghazlan G, Caperaa S, Petit C (1995) An incremental formulation for the linear analysis of thin viscoelastic structures using generalized variables. *Int J Numer Methods Eng* 38:3315-3333.
- Humphrey PE (1982) Physical aspects of wood particleboard manufacture. PhD thesis, University of Wales, Wales, UK.
- Humphrey PE, Bolton AJ (1989) The hot pressing of dry-formed wood-based composites. Part II. A simulation model for heat and moisture transfer and typical results. *Holzforschung* 43(3):199-206.
- Kamke FA, Wolcott MP (1991) Fundamentals of flakeboard manufacture: Wood-moisture relationships. *Wood Sci Technol* 25:57-71.
- Kavazović Z (2011) *Modélisation mathématique du passage à chaud des panneaux MDF: Couplage du modèle mécanique avec le modèle couplé de transfert de chaleur et de masse*. PhD thesis, Université Laval, Québec, Canada. 145 pp. <http://www.giref.ulaval.ca/publications/memoires-et-theses.html> (February 16, 2012).
- Kavazović Z, Deteix J, Cloutier A, Fortin A (2010) Sensitivity study of a numerical model of heat and mass transfer involved during the MDF hot pressing process. *Wood Fiber Sci* 42(2):130-149.
- Kavvouras PK (1977) Fundamental process variables in particleboard manufacture. PhD thesis, University of Wales, Wales, UK. 156 pp.
- Lee JN, Kamke FA, Watson LT (2007) Simulation of the hot-pressing of a multi-layered wood strand composite. *J Composite Mater* 41(7):879-904.
- Nigro N, Storti M (2001) Hot-pressing process modeling for medium density fiberboard (MDF). *Int J Math* 26(12):713-729.
- Pereira C, Carvalho LMH, Costa CAV (2006) Modeling the continuous hot-pressing of MDF. *Wood Sci Technol* 40:308-326.
- Reddy JN (2006) *An introduction to the finite element method*. 3rd ed. McGraw Hill, Higher Education, New York, NY. 766 pp.
- Siau J (1984) *Transport processes in wood*. Springer-Verlag, New York. 245 pp.
- Thömen H (2000) Modeling the physical process in natural fiber composites during batch and continuous pressing. PhD thesis, Oregon State University, Corvallis, OR. 187 pp.
- Thömen H, Haselein CR, Humphrey PE (2006) Modeling the physical process relevant during hot pressing of wood-based composites. Part 2. Rheology. *Holz Roh Werkst* 64:125-133.
- Thömen H, Humphrey PE (2003) Modeling the continuous pressing process for wood-based composites. *Wood Fiber Sci* 35(3):456-468.
- Thömen H, Humphrey PE (2006) Modeling the physical process relevant during hot pressing of wood-based composites. Part 1. Heat and mass transfer. *Holz Roh Werkst* 64:1-10.
- Thömen H, Ruf C (2008) Measuring and simulating the effects of the pressing schedule on the density profile development in wood-based composites. *Wood Fiber Sci* 40(3):325-338.
- von Haas G (1998) Untersuchungen zur Heißpressung von Holzwerkstoffmatten unter besonderer Berücksichtigung des Verdichtungsverhaltens der Permeabilität der Temperaturleitfähigkeit und der Sorptionsgeschwindigkeit. PhD thesis, Hamburg University, Germany. 264 pp.
- von Haas G, Frühwald A (2000) Untersuchungen zur Verdichtungsverhalten von Faser- Span- und OSB-Matten. *Holz Roh Werkst* 58:317-323.
- Wang S, Winistorfer PM (2000a) Consolidation of flakeboard mats under theoretical laboratory pressing and simulated industrial pressing. *Wood Fiber Sci* 32(4):527-538.
- Wang S, Winistorfer PM (2000b) Fundamentals of vertical density profile formation in wood composites. Part 2. Methodology of vertical density formation under dynamic conditions. *Wood Fiber Sci* 32(2):220-238.
- Wang S, Winistorfer PM, Young TM (2004) Fundamentals of vertical density profile formation in wood composites. Part 3. MDF density formation during hot-pressing. *Wood Fiber Sci* 36(1):17-25.
- Wang S, Winistorfer PM, Young TM, Helton C (2001a) Step-closing pressing on medium density fiberboard. Part 1. Influences on the vertical density profile. *Holz Roh Werkst* 59:19-26.
- Wang S, Winistorfer PM, Young TM, Helton C (2001b) Step-closing pressing on medium density fiberboard. Part 2. Influences on panel performance and layer characteristics. *Holz Roh Werkst* 59:311-318.
- Winistorfer PM, Moschler WW Jr., Wang S, DePaula E, Bledsoe BL (2000) Fundamentals of vertical density profile formation in wood composites. Part 1. In-situ density measurement of the consolidation process. *Wood Fiber Sci* 32(2):209-219.
- Winistorfer PM, Young TM, Walker E (1996) Modeling and comparing vertical density profiles. *Wood Fiber Sci* 28(1):133-141.
- Wolcott MP, Kamke FA, Dillard DA (1990) Fundamentals of flakeboard manufacture: Viscoelastic behavior of the wood component. *Wood Fiber Sci* 22(4):345-361.
- Yu C, Dai C, Wang BJ (2007) Heat and mass transfer in wood composite panels during hot pressing. Part 3. Predicted variations and interactions of the pressing variables. *Holzforschung* 61:74-82.
- Zombori BG, Kamke FA, Watson LT (2003) Simulation of the internal conditions during the hot-pressing process. *Wood Fiber Sci* 35(1):2-23.
- Zombori BG, Kamke FA, Watson LT (2004) Sensitivity analysis of internal mat environment during hot pressing. *Wood Fiber Sci* 36(2):195-209.

APPENDIX 1

The fourth-order elasticity tensor E can be written as a 6×6 symmetric matrix and a relation between stress and strain can be expressed as follows:

$$\begin{pmatrix} \sigma_1 \\ \sigma_2 \\ \sigma_3 \\ \sigma_{23} \\ \sigma_{13} \\ \sigma_{12} \end{pmatrix} = \begin{pmatrix} \frac{1 - \nu_{23}\nu_{32}}{E_2E_3S} & \frac{\nu_{21} + \nu_{23}\nu_{31}}{E_2E_3S} & \frac{\nu_{31} + \nu_{21}\nu_{32}}{E_2E_3S} & 0 & 0 & 0 \\ \frac{\nu_{21} + \nu_{23}\nu_{31}}{E_2E_3S} & \frac{1 - \nu_{31}\nu_{13}}{E_1E_3S} & \frac{\nu_{23} + \nu_{21}\nu_{13}}{E_1E_2S} & 0 & 0 & 0 \\ \frac{\nu_{31} + \nu_{21}\nu_{32}}{E_2E_3S} & \frac{\nu_{23} + \nu_{21}\nu_{13}}{E_1E_2S} & \frac{1 - \nu_{21}\nu_{12}}{E_1E_2S} & 0 & 0 & 0 \\ 0 & 0 & 0 & G_{23} & 0 & 0 \\ 0 & 0 & 0 & 0 & G_{13} & 0 \\ 0 & 0 & 0 & 0 & 0 & G_{12} \end{pmatrix} \begin{pmatrix} \epsilon_1 \\ \epsilon_2 \\ \epsilon_3 \\ \epsilon_{23} \\ \epsilon_{13} \\ \epsilon_{12} \end{pmatrix} \tag{11}$$

with $S = \frac{1}{E_1E_2E_3} (1 - 2\nu_{21}\nu_{32}\nu_{13} - \nu_{13}\nu_{31} - \nu_{23}\nu_{32} - \nu_{12}\nu_{21})$. The different parameters depend on temperature T and moisture M first through the relation

$$E_{el} = 1.515 \cdot 10^4 \exp\left\{A + \rho_{MAT} \cdot \exp(B) - \ln\left(\frac{\rho_{MAT}}{198.3}\right)\right\} \tag{12}$$

with

$$A = a_1 \cdot M \cdot 100 + b_1 \cdot (T - 273.15) + c_1;$$

$$B = a_2 \cdot M \cdot 100 + b_2 \cdot (T - 273.15) + c_2$$

and where the constants $a_i, b_i, c_i (i = 1, 2)$ can be found in von Haas (1998) and Thömen et al (2006):

$$a_1 = 4.22 \cdot 10^{-2}, b_1 = -2.74 \cdot 10^{-2}, c_1 = 3.25$$

$$a_2 = -1.86 \cdot 10^{-2}, b_2 = 3.24 \cdot 10^{-3}, c_2 = -5.10$$

Assuming MDF as a plane isotropic material and directions X and Y (1 and 2) to be the plane of isotropy, we further have $E_1 = E_2$, $G_{23} = G_{13}$, $G_{12} = \frac{E_1}{2(1 + \nu_{12})}$, $\nu_{12} = \nu_{21}$, $\nu_{23} = \nu_{32} = \nu_{13} = \nu_{31}$ (Ganev et al 2005). We also assumed that the elasticity coefficients depended on the resin cure degree α (defined in Part 1) as

$$E_1 = E_2 = E_{el} \cdot (1 + 32 \cdot \alpha); E_3 = E_{el} \tag{13}$$

Variation of the Poisson coefficient is a delicate issue. We defined the time of the first compaction t_{fc} as the moment in time when the mat reached 1.9 times its final thickness. That was the moment when we estimated that the mat gained sufficient cohesion level and set its Poisson's ratio to a nominal value (which in our case was 0.25). We therefore set

$$Poisson = \begin{cases} 0.25 \cdot F_1 & F_1 \leq 1 \\ 0.25 & F_1 > 1 \end{cases} \tag{14}$$

$$F_1 = 2.13 \cdot \left[1 - \frac{1}{\sqrt{b}}\right] \tag{15}$$

where

$$b = 1 + 7 \cdot \exp\left(27 \cdot \left[\frac{t}{t_{fc}} - 1\right] - 1\right)$$

In the case of our laboratory pressing schedule, t_{fc} was estimated at 35 s. Evolution in time of the resulting Poisson's coefficient can be seen in Fig 2b. Finally, we set

$$\nu_{12} = \nu_{23} = Poisson \tag{16}$$

$$G_{12} = \frac{E_1}{2 \cdot (1 + Poisson)};$$

$$G_{13} = G_{23} = \frac{E_3}{2 \cdot (1 + Poisson)} \tag{17}$$

Parameters related to heat and mass transfer model were presented in Part 1 of this study.